



## 3D microstructure modeling of compressed fiber-based materials



Gerd Gaiselmann<sup>a,\*</sup>, Christian Tötze<sup>b,c</sup>, Ingo Manke<sup>b</sup>, Werner Lehnert<sup>d,e</sup>,  
Volker Schmidt<sup>a</sup>

<sup>a</sup> Institute of Stochastics, Ulm University, 89069 Ulm, Germany

<sup>b</sup> Institute of Applied Materials, Helmholtz Centre Berlin for Materials and Energy (HZB), 14109 Berlin, Germany

<sup>c</sup> Department of Materials Science and Technology, Technische Universität Berlin, 10623 Berlin, Germany

<sup>d</sup> Institute of Energy and Climate Research, IEK-3: Electrochemical Process Engineering, Forschungszentrum Jülich, 52425 Jülich, Germany

<sup>e</sup> Modeling in Electrochemical Process Engineering, RWTH Aachen University, 52062 Aachen, Germany

### HIGHLIGHTS

- Introduction of model describing uniaxially compressed fiber-based materials.
- It allows to virtually generate realistically compressed gas-diffusion layers (GDL).
- Compression model is combined with a model for uncompressed non-woven GDL.
- This allows to efficiently generate compressed GDL in arbitrary 3D volumes.

### ARTICLE INFO

#### Article history:

Received 21 August 2013

Received in revised form

30 December 2013

Accepted 10 January 2014

Available online 29 January 2014

#### Keywords:

Compression model  
Fiber-based materials  
Gas-diffusion layer  
PEMFC  
Simulated annealing  
Stochastic modeling

### ABSTRACT

A novel parametrized model that describes the 3D microstructure of compressed fiber-based materials is introduced. It allows to virtually generate the microstructure of realistically compressed gas-diffusion layers (GDL). Given the input of a 3D microstructure of some fiber-based material, the model compresses the system of fibers in a uniaxial direction for arbitrary compression rates. The basic idea is to translate the fibers in the direction of compression according to a vector field which depends on the rate of compression and on the locations of fibers within the material. In order to apply the model to experimental 3D image data of fiber-based materials given for several compression states, an optimal vector field is estimated by simulated annealing. The model is applied to 3D image data of non-woven GDL in PEMFC gained by synchrotron tomography for different compression rates. The compression model is validated by comparing structural characteristics computed for experimentally compressed and virtually compressed microstructures, where two kinds of compression – using a flat stamp and a stamp with a flow-field profile – are applied. For both stamps types, a good agreement is found. Furthermore, the compression model is combined with a stochastic 3D microstructure model for uncompressed fiber-based materials. This allows to efficiently generate compressed fiber-based microstructures in arbitrary volumes.

© 2014 Elsevier B.V. All rights reserved.

### 1. Introduction

We introduce a novel parametrized model that describes the 3D microstructure of compressed fiber-based materials. This model is of high practical relevance since it allows for generating the microstructure of gas-diffusion layers (GDL) under consideration of compression conditions as found in fuel cells. Given the input of a 3D microstructure of some (uncompressed) fiber-system, the model compresses the system of fibers in a uniaxial direction. By

the term ‘uniaxial compression’ we mean that the material, located on a fixed ground, is compressed by a stamp which presses the material from a uniaxial direction against the fixed ground, see Fig. 1. The compression rate is then given by 1 minus the ratio of the thickness of the compressed material and the thickness of the uncompressed material. The model can be applied to mimic any uniaxial compression of fiber-based materials. In particular, it is able to describe the compression for varying stamp geometries and for arbitrary compression rates. In addition, when applied to systems of non-overlapping fibers, i.e. fibers which do not penetrate each other, the compression model keeps the fiber system free of overlaps and it preserves the total volume of the fibers. Note that the idea of the compression model introduced in the present paper

\* Corresponding author. Tel.: +49 731 50 23590; fax: +49 731 50 23649.

E-mail addresses: [gerd.gaiselmann@uni-ulm.de](mailto:gerd.gaiselmann@uni-ulm.de), [gerdga@gmx.de](mailto:gerdga@gmx.de) (G. Gaiselmann).

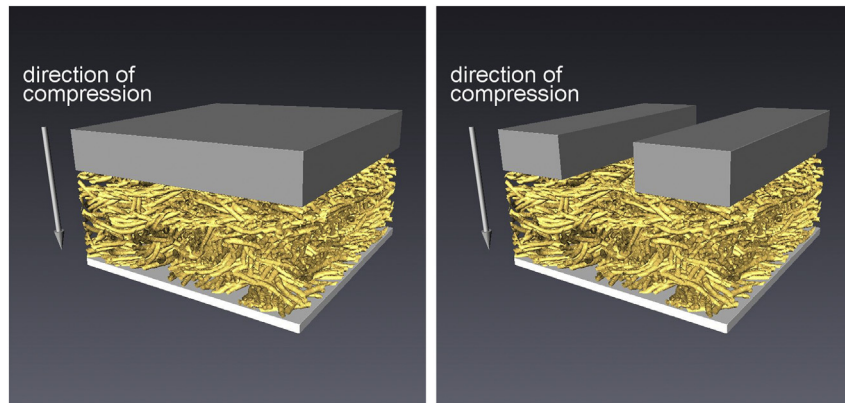


**Fig. 1.** 3D image of non-woven GDL (yellow fibers) with flat stamp (left) and with stamp of flow-field structure (right).

is to rebuild the structure of compressed materials, i.e., it is a purely morphological approach which does not include any physics. The advantage of this morphological approach is that compression of materials can be mimicked by means of simulations in short time on huge domains and additionally the simulations based on the compression model are good approximations of real compressed materials.

We apply the compression model to 3D image data describing the microstructure of non-woven GDL in proton exchange membrane fuel cells (PEMFC), which consists of (non-overlapping) fibers. PEMFC are a seminal technology for electrical power generation due to their high efficiency and environment friendly emissions [1,2]. An important factor for the efficiency and stability of the PEMFC is its GDL, which is mainly responsible for the gas supply of the electrodes and water storage/evacuation within the GDL. For further details concerning the functionality of GDL we refer e.g. to [3–7]. The GDL under examination is a porous material whose solid phase consists of a system of strongly curved (non-overlapping) carbon fibers. The microstructure of the GDL is closely related to its functionality, in particular to the transportation of gases and fluids through the GDL [8–12]. Thus, the systematic development of ‘designed’ morphologies with improved functionality is an important, but largely unsolved task.

In the operating state of PEMFC, the GDL is uniaxially compressed under the lands of the flow-field in order to ensure the mechanical support of the membrane as well as thermal and electrical conductivity. It was demonstrated that the compression rate of the GDL influences the performance of a PEMFC [13–17]. In Fig. 1 (right), the microstructure of a non-woven GDL is displayed with a stamp possessing a flow-field structure. In order to improve the understanding of transportation processes within the GDL in operating PEMFC, it is of great importance to investigate the correlation between compressed microstructures of GDL and the corresponding physical processes, e.g. gas and water transport.

The first step towards the analysis of this correlation is to understand how the microstructure changes under compression. In particular, there is a need of models describing the 3D microstructure of compressed GDL by the flow-field for varying rates of compression.

In general, there exist two classes of models which virtually compress microstructures. The first class is based on numerical simulations which rebuild the geometry of the mechanical compression by solving some differential equations (e.g. compression of spherical aggregates). In contrast, the second class represents a purely geometrical approach which does not include any physics and only aims to realistically rebuild compressed

microstructures. Since the compression of microstructures needs extensive computational time for physical models and thus limits the volumes or resolution that can be handled, we focus on the second class of compression models in the following. Furthermore, within this class, we restrict ourselves to uniaxial compression. In literature, there exist some models for uniaxial compression of fiber-based materials, cf. [18–20]. In Ref. [19], a compression model is proposed which mimics compression by a flat stamp only for multi-layer structures, i.e., consisting of stacked layers. In Refs. [18,20], a further compression model is presented which allows to uniaxially compress a given 3D microstructure of some fiber-based materials by a flat stamp where the microstructure is represented by a 3D image. So far, to the best of the authors’ knowledge, there exists no purely geometrically motivated compression model which describes uniaxial compression for arbitrary stamp geometries. However, in reality the GDL is compressed by a flow-field stamp. A stamp which mimics this structure is shown in Fig. 1 (right). Note that there are dramatic structural differences when compressing the GDL either with a flat stamp or with a stamp possessing a flow-field structure. Thus, there is a need for more general compression models in order to analyze the influence of compression by flow-field stamps on transportation properties of the GDL. To fill this gap, we present a model which is able to describe all kinds of uniaxial compression, in particular compression by a flow-field-like stamp as occurring for GDL in operating PEMFC. More precisely, given the input of a 3D microstructure of some fiber-system, the model uniaxially compresses the system of fibers for arbitrary stamp geometries and for arbitrary compression rates. The compression model is constructed by means of a two-stage approach. The basic idea of the model is to translate the fibers in the direction of compression according to a vector field  $V_c$  which depends on the compression rate  $c$  and on the location of the fibers within the material. Subsequently, an avoidance algorithm is applied to the translated fiber system which prevents the mutual penetration of fibers and preserves their lengths. Thus, the proposed compression model generalizes the model described in Ref. [20] in two ways: 1) to arbitrary stamp geometries, and 2) it keeps non-overlapping fibers free of overlaps. Moreover, an estimation technique for the optimal vector field in order to fit it to experimental data is introduced which is based on simulated annealing.

To validate the model, it is applied to the 3D microstructure of non-woven GDL in PEMFC gained by synchrotron tomography for four different compression rates  $c \in \{0, 10, 20, 30\}$  (in %). Thereby, we distinguish between two kinds of compression: 1) using a flat stamp, and 2) a stamp possessing a flow-field structure. Note that when the compression model is applied to systems of non-overlapping fibers,

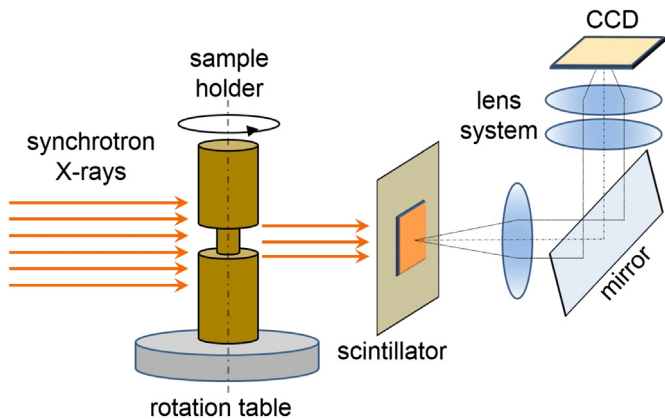


Fig. 2. Scheme of the principal experimental set up at the tomographic instrument.

single fibers need to be *identified* in order to separate them from each other. Such a *single-fiber extraction* can be done efficiently by the algorithm introduced in Ref. [21]. The compression model is validated by comparing structural characteristics computed for experimentally and virtually compressed microstructures. For both types of stamps, a good agreement between experimental and virtual compression is found.

In a second step, we apply the compression model to virtual microstructures of uncompressed non-woven GDL, which are generated according to a stochastic 3D simulation model introduced in Ref. [22]. The combination of the stochastic microstructure model with the compression model allows to realistically simulate compressed GDL on an arbitrary large scale for arbitrary compression rates. Since the access to tomography images is limited or often, only images of uncompressed media are available, the combination of both models enables us to efficiently generate a large number of virtual (but realistic) microstructure scenarios for compressed GDL. When employed in fuel cell simulation, this model provides great flexibility: the microstructure of GDL can be easily adapted to different degrees of compression in order to study the influence of clamping pressure on fuel cell operation. Furthermore, it allows for studying different flow-field geometries while the volume of the generated GDL-structure can be conveniently adjusted to meet the desired requirements. By systematically varying the parameters of the compression model (describing the

3D microstructure of compressed GDL), new virtual GDL can be generated and in combination with computational transport simulations, the microstructure-functionality relationship of the GDL in operating PEMFC can be investigated. In this way, the systematic design of morphologies with improved functionality based on computer experiments can be achieved.

The paper is organized as follows. Section 2 briefly describes the material investigated in this paper and the set-up for the generation of 3D image data. In Section 3, the compression model is introduced and the estimation technique for its parameter is presented. Subsequently, in Section 4, the compression model is applied to synchrotron data of non-woven GDL for different compression rates, where we distinguish between two kinds of compression, i.e., using a flat stamp and a stamp possessing a flow-field structure. Section 5 combines a stochastic simulation model for uncompressed non-woven GDL with the compression model introduced in the present paper. Finally, Section 6 summarizes the results and provides a short outlook regarding possible future research.

## 2. Imaging and material

A prominent example of a fiber-based material is the GDL in PEMFC where the consideration of compressed GDL is of great importance since the GDL is compressed in the operating state of PEMFC. Therefore, 3D image data of uncompressed and compressed non-woven GDL are needed [23], where we distinguish between compression by a flat and by a flow-field-like stamp, see Figs. 3 and 4. Thus, in this section, we briefly discuss the imaging technique used in Ref. [23] to record compressed microstructures and we give some details about the material considered. Finally, we shortly discuss an algorithm which automatically extracts a system of single fibers from tomographic 3D images. This algorithm allows the direct application of the compression model, introduced in Section 3, to experimental image data of fiber-based materials.

### 2.1. Imaging technique

The imaging experiments were performed at the Helmholtz-Zentrum Berlin using the synchrotron tomography station of the BAMline which is located at the synchrotron source BESSY (Berlin/Germany) [24]. The high brilliance of the synchrotron X-ray beam allows producing tomographic data of superior quality in terms of

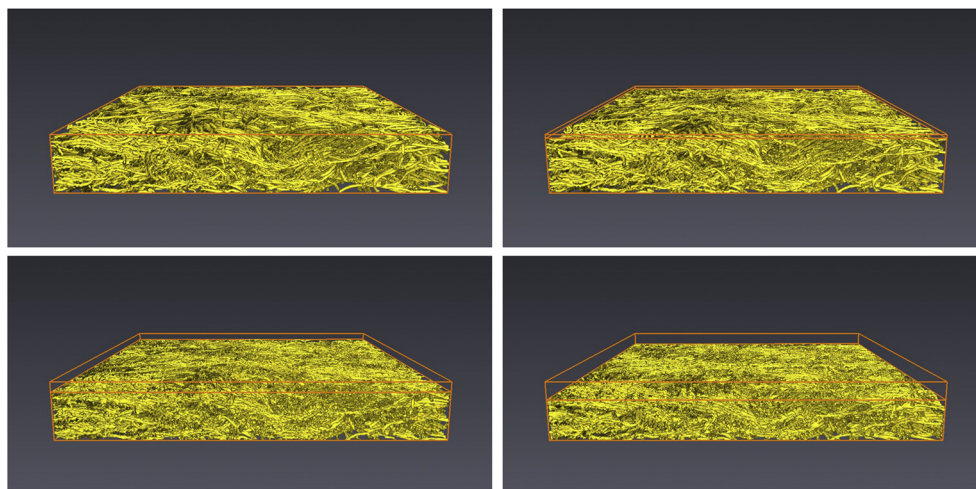
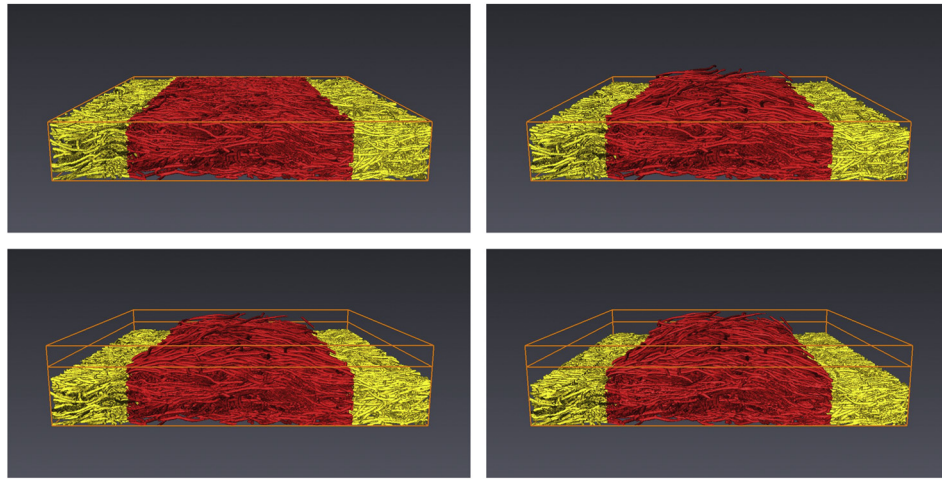


Fig. 3. 3D image data gained by synchrotron tomography of non-woven GDL compressed by a flat stamp with compression rates  $c = 0\%$  (top left),  $c = 10\%$  (top right),  $c = 20\%$  (bottom left) and  $c = 30\%$  (bottom right).



**Fig. 4.** 3D image data gained by synchrotron tomography of non-woven GDL compressed by a flow-field stamp with compression rates  $c = 0\%$  (top left),  $c = 10\%$  (top right),  $c = 20\%$  (bottom left) and  $c = 30\%$  (bottom right). The red (yellow) marked fibers are located underneath the channel (the rips of the flow-field stamp). (For interpretation of the references to color in this figure legend, the reader is referred to the web version of this article.)

resolution and contrast [23,25,26]. This way, smallest details of the three-dimensional GDL structure such as shape and course of individual carbon fibers can be accurately rendered. The principal set up of the tomographic measurement is displayed in Fig. 2.

A W–Si double multilayer monochromator with an energy resolution of  $\Delta E/E = 10^{-2}$  was used to obtain a monochromatic X-ray beam. The beam energy was adjusted to 15 keV in order to achieve optimal contrast for fibers. Images were captured with a  $4008 \times 2672$  pixel<sup>2</sup> camera set-up (PCO camera with a Gadox scintillator screen) rendering a field of view of  $3.3 \times 2.2$  mm<sup>2</sup> with a pixel size of 0.876  $\mu\text{m}$  and a respective physical spatial resolution of about 2  $\mu\text{m}$  [27]. Circular GDL samples with diameters of 3 mm were adjusted in the sample holder and mounted on a translation/rotation unit. For each tomogram, samples were rotated in equidistant steps covering an angular range of 180°. A radiographic set of 1500 projections and 500 flatfields was taken and, subsequently, reconstructed to a 3D volume. The exposure time is 2.5 s plus 1.7 s read-out for a single radiograph adding up to an acquisition time of 140 min for the complete tomogram. The measurements were performed using a dedicated compression device as sample holder which provides well-defined compression conditions and meets the instrumental requirements, e.g. in terms of sufficient beam transmission. The compression device is able to compress GDL by different stamp types (see Figs. 3 and 4), in particular, for a flat stamp and a stamp consisting of a flow-field structure, where the width of the flow-field canal is 790  $\mu\text{m}$ .

## 2.2. Description of material

The application of the compression model, introduced in the present paper, is based on tomographic data of the GDL type H2315, a non-woven, carbon fiber-based material produced by the company Freudenberg FFCCT. This material does not contain binder, wet proofing agents nor a micro porous layer (MPL). H2315 is used as standard material for many fuel cell applications. Note, however, that it is usually equipped with wet proofing agent and/or MPL in order to adapt its physical properties to the requirements of the respective application.

## 2.3. Fiber extraction algorithm

The experimental 3D image data gained by synchrotron tomography displays the (uncompressed and compressed) non-

woven GDL by a matrix of voxels. In the following, we extract the systems of fibers from the tomographic 3D image data of uncompressed GDL. Thereby, the complexity of data is reduced since it is represented by thousands of fibers (approximated by polygonal tracks which are given in Euclidean coordinates) instead of millions of voxels. Furthermore, the input data of the compression model introduced in this paper are uncompressed fiber-systems and thus it can be directly applied to the extracted fibers of uncompressed non-woven GDL.

We briefly describe an algorithm to automatically detect single fibers from 3D tomographic data of fiber-based materials which has been proposed in Ref. [21]. The algorithm yields the extracted center lines of individual fibers which are approximated by polygonal tracks. Since in experimental data there occur irregularities like noise or binarization artefacts it is only possible to extract parts of the center lines. Then, a stochastic optimization algorithm connects these fragments of the center lines to each other such that the complete fibers are correctly reconstructed. For further information see Ref. [21]. Exemplarily, we have applied the algorithm to experimental image data of uncompressed non-woven GDL. The experimental data and its extracted fiber system are in an excellent optical accordance, see Fig. 5.

## 3. Compression model for fiber-based materials

In this section, we introduce a parametrized model that describes the 3D microstructure of compressed materials. Given the input of an uncompressed 3D microstructure of a two-phase material consisting of an uncompressed solid phase and a pore phase, the model compresses the solid phase in a uniaxial direction for arbitrary compression rates. When speaking of a 3D microstructure, we refer to a segmented tomographic 3D image or synthetic 3D images drawn e.g. from stochastic simulation models. To make the model more accessible, we constrict it and its range of application to materials consisting of non-overlapping systems of fibers. But note that by slight modifications, the model can be extended to other types of materials, including composite materials. The compression model introduced in the following should possess several properties. In particular, the model should

- 1) describe different uniaxial compression processes on the microstructure of fiber-based materials realistically, where it should describe the compression of fiber-based materials

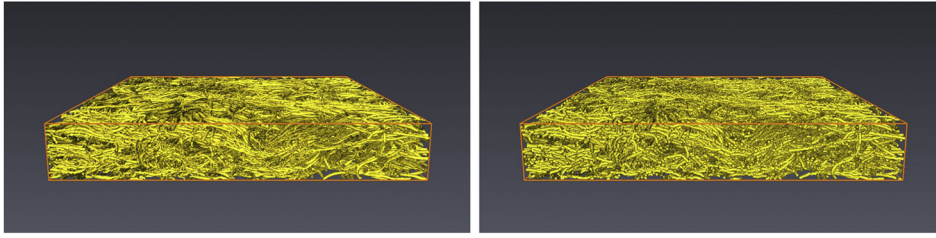


Fig. 5. 3D image of uncompressed GDL (left) and its extracted system of single fibers (right).

accomplished by different stamp geometries, e.g. by a flat stamp or by a stamp with a flow-field structure, see also Fig. 1.

- 2) preserve the non-overlapping of fibers.
- 3) describe compressed microstructures of fiber-based materials with continuous compression rates  $c \in [0, c_{\max})$ , where  $c_{\max} < 1$  is the largest compression rate such that it is possible to preserve a non-overlapping fiber-system after applying the compression model.
- 4) be a volume preserving operation, i.e., the total volume of fibers should remain constant under compression.

In the following, we first introduce the compression model for fiber-based materials. Then, a fitting procedure of its parameters is discussed when the uncompressed and several compressed microstructures of a fiber-based material are given.

### 3.1. Model description

We now introduce a compression model which describes uniaxially compressed microstructures of fiber-based materials. Throughout this paper, we assume that microstructures are compressed in a uniaxial direction, say, the  $z$ -direction. Consequently, we assume that the fibers are only shifted in the direction of compression, but the magnitude of the shift may vary in space. To motivate the assumption, consider Fig. 6 displaying a cross-section of a fiber system (GDL) in an uncompressed state (left) and a compressed state (right). It can clearly be seen that fibers are mainly shifted in  $z$ -direction. Note that due to binarization artefacts and irregularities of the imaging of the material, it is implausible to obtain a perfect translation in  $z$ -direction even if 100% of the fibers were shifted in  $z$ -direction. On the other hand, it is intuitively clear that fibers are translated to a large part only in  $z$ -direction when considering the case of uniaxial compression. For these reasons, we neglect possible translations of fibers in other directions.

The compression model is constructed by means of a two-stage approach. First, the fibers are translated in the direction of

compression according to a vector field  $V_c$  depending on the compression rate  $c \in [0, c_{\max})$ . Note that each fiber is represented by a polygonal track. To the starting and endpoints of each segment of the polygonal tracks, the vector field assigns a transition vector, which depends on the location of the point within the material. The translation of the fibers according to the vector field  $V_c$  may yield overlaps in the fiber system and increase or decrease the length of individual fibers. Therefore, in a second step, we apply an iterative avoidance algorithm [28] to the translated fiber system which transforms the translated fiber system to a non-overlapping fiber system, where the length and curvature of the fibers are preserved.

#### 3.1.1. Translation algorithm

Let  $\Xi = \bigcup_{i=1}^{\infty} F_i \oplus B(0, r) \subset \mathbb{R} \times \mathbb{R} \times [0, z_{\max}]$  be a system of fibers (representing a fiber-based material) and let  $F_i$ ,  $i = 1, 2, \dots$  be polygonal tracks approximating single fibers, i.e.,  $F_i$  is a system of line segments defined by

$$F_i = \bigcup_{j=1}^{n_i} \ell_{ij},$$

where

$$\ell_{ij} = (p_{ij}^{(1)}, p_{ij}^{(2)}) \in \mathbb{R}^{3 \times 2}$$

is the  $j$ th line segment of the  $i$ th fiber consisting of starting and endpoints  $p_{ij}^{(1)}, p_{ij}^{(2)} \in \mathbb{R}^3$  with Euclidean length  $|\ell_{ij}| = r/4$ . Moreover,  $z_{\max} > 0$ ,  $r$  defines the constant radius of the fibers,  $B(0, r)$  the (three-dimensional) sphere with origin as center point and radius  $r$ , and  $\oplus$  denotes the Minkowski addition. Thus, we identify the microstructure of a fiber-based material with the union set of all fibers, where each fiber is represented by a system of connected line segments. Given this representation, we can now describe the compression of fibers in more detail. Let  $V_c : \mathbb{R} \times \mathbb{R} \times [0, z_{\max}] \rightarrow \mathbb{R}$  be a continuous vector field with the constraints that  $V_c(x, y, 0) = 0$  for all  $(x, y)^T \in \mathbb{R}^2$ , and  $V_c(x, y, z) \leq z$  for all  $(x, y)^T \in \mathbb{R}^2$  and  $0 \leq z \leq$

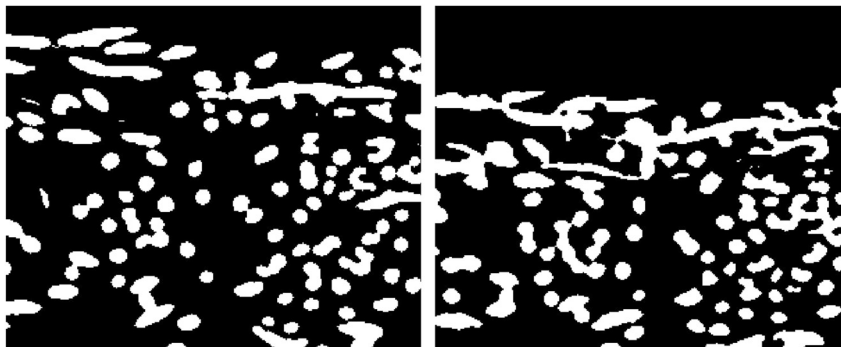


Fig. 6. Cross-section view on non-woven GDL in uncompressed state (left) and in compressed state with  $c = 20\%$ .

$z_{\max}$ . In the first stage, the system of fibers  $\Xi$  is translated according to the vector field  $V_c$  which yields the *translated system of fibers*, denoted by  $\Xi'$ , where

$$\Xi' = \bigcup_{i=1}^{\infty} F'_i \oplus B(0, r), \quad \text{with} \quad F'_i = \bigcup_{j=1}^{n_i} \ell'_{ij} \quad \text{and} \\ \ell'_{ij} = \left( p_{ij}^{(1)} - V_c(p_{ij}^{(1)}), p_{ij}^{(2)} - V_c(p_{ij}^{(2)}) \right).$$

Thus, the translation of the fiber system is described by translating the starting and endpoints of each line segment of the fibers. In a second step, an avoidance-algorithm is applied to the translated system of fibers  $\Xi'$ , in order to de-overlap the system of fibers. The resulting microstructure is denoted by  $\Xi''$ . Note that the compressed microstructure  $\Xi''(c)$  as well as the translated fiber system  $\Xi'(c)$  are located in the set  $W_c$ , where  $W_c = \{(x, y, z) \in \mathbb{R}^3 : (x, y) \in \mathbb{R}^2, z \in [0, z_{\max} - V_c(x, y, z_{\max})]\}$ . In the following, we shortly discuss the iterative avoidance algorithm introduced in Ref. [28].

### 3.1.2. Iterative avoidance algorithm

To obtain a system of compressed and non-overlapping fibers, the translated fiber system  $\Xi'$  described in Section 3.1.1 is further transformed. Recall that  $r$  denotes the thickness of the fibers. The principle idea is to first represent each fiber by a chain of (overlapping) spheres where the spheres have the same radius  $r$  equal to the fiber thickness and their midpoints are located equidistantly (with distances  $r/4$  from each other) on the line segments of the fibers, see also Fig. 7 (left and center). Using this representation, the basic idea is to translate the midpoints of the spheres such that no spheres from different fibers overlap, see Fig. 7 (right).

In more detail, in every iteration step  $i$ , each midpoint  $M_n^{(i)} \in \mathbb{R}^3$  of those spheres is translated by a vector  $t = t_1 + t_2$ , i.e.,

$$M_n^{(i+1)} = M_n^{(i)} + t = M_n^{(i)} + t_1 + t_2.$$

The translation function  $t_1$  separates overlapping spheres which belong to different chains of spheres by moving them away from each other, and the second translation  $t_2$  preserves the distance and the angle between neighboring spheres belonging to the same chain of spheres (and thus the length and curvature of the fibers). For the application of the compression model within the present paper, the function  $t_1$  is weighted stronger than  $t_2$  as proposed in Ref. [28], i.e., to keep fibers non-overlapping is more important than preserving their curvatures and lengths. Note that if considering compression of fiber-based materials where the elasticity of fibers is strongly restricted, i.e., large bending of fibers is not realistic without cracking, the weighting of functions  $t_1$  and  $t_2$  can be adopted accordingly. In this case, the fibers would not be allowed to exceed a certain bending. If after an iteration step  $i$ , a midpoint  $M_n^{(i)} = (m_{n,x}^{(i)}, m_{n,y}^{(i)}, m_{n,z}^{(i)})^T$  is not located in  $W_c$ , it is set to the point given by the closest distance with respect to the  $z$ -coordinate, i.e., if  $M_n^{(i)} \notin W_c$  we set  $M_n^{(i)} = \operatorname{argmin}_{(m_{n,x}^{(i)}, m_{n,y}^{(i)}, z) \in W_c} |z - m_{n,z}^{(i)}|$ . For further

information regarding the iterative avoidance algorithm, the reader is referred to [28]. The final system of non-overlapping fibers is denoted by  $\Xi''(c)$ .

### 3.2. Fitting of vector field $V_c$ for fixed compression rate $c$

So far, the compression model has been introduced which is uniquely determined by the parameters of the continuous vector field  $V_c$ . It remains, however, unclear which choice of  $V_c$  is most suitable to describe compression of fiber-based materials in a realistic way. Therefore, in this section, we introduce a *fitting procedure* which estimates the continuous vector field  $V_c$  of the compression model described in Section 3.1 for any given value of  $c \in [0, c_{\max})$ . For this procedure, 3D image data of one and the same fiber system in both, an uncompressed and a compressed state, is required. The estimation technique is based on the fact that the total volume of the fiber system must remain constant under compression, since fibers cannot overlap. More precisely, the idea is to choose a vector field such that the translated fiber system  $\Xi''$  matches the compressed fiber system observed in experimental data as good as possible. Since we cannot expect a perfect match of these fiber systems due to e.g. binarization artefacts, this procedure optimizes the match of local distributions of fibers in the virtually compressed and the experimentally compressed microstructures. In particular, we subdivide the uncompressed and compressed microstructures in small (pairwise disjoint) cuboids and minimize the absolute values of the differences of the total fiber volumes in corresponding cuboids for uncompressed and compressed data. To solve this optimization problem we use simulated annealing, a well-known stochastic optimization algorithm.

#### 3.2.1. Optimization problem

Let us assume that we consider the uncompressed microstructure in the 3D volume  $W_0 \subseteq \mathbb{R}^3$  and the compressed microstructure in  $W_1 \subseteq \mathbb{R}^3$ . Furthermore, we assume that the dimension in  $x$ - and  $y$ -direction of  $W_0$  and  $W_1$  are the same but by the uniaxial compression the dimensions in  $z$ -direction are allowed to vary, see Fig. 8a. In a first step, the observation windows  $W_0$  and  $W_1$  are subdivided in the same number of small disjoint cuboids, where the side length of the cuboids are equal in  $x$ - and  $y$ -direction for  $W_0$  and  $W_1$  but differ in  $z$ -direction, see Fig. 8b. Note that the decomposition of  $W_0$  and  $W_1$  is much finer than displayed in Fig. 8b.

Given the decomposition of  $W_0$  and  $W_1$ , we now consider a single pair of stacks of cuboids, as displayed in Fig. 8c (left). We denote both stacks by  $S' = (z'_0, \dots, z'_n)$  and  $S = (z_0, \dots, z_n)$  with corresponding total volumes of fibers within the cuboids given by  $(V'_1, \dots, V'_n)$  and  $(V_1(z_0, \dots, z_n), \dots, V_n(z_0, \dots, z_n))$ , respectively. Since we assume that fibers are only translated in  $z$ -direction, the total fiber volume of both stacks must be the same. Thus, the fibers have to be compressed in such a way that the fiber volume of each cuboid in the uncompressed microstructure is the same as the fiber volume of the corresponding cuboid in the compressed

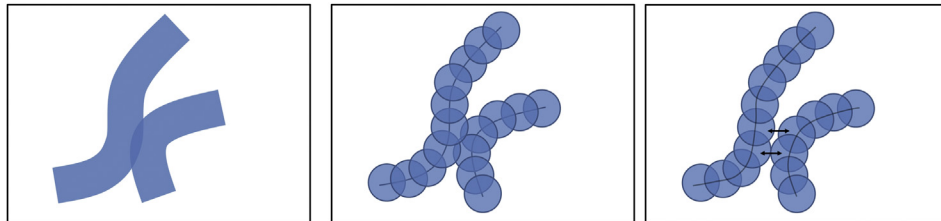


Fig. 7. Schematic 2D visualization of a fiber system (left) being represented by overlapping spheres (center) and subsequently translated to a system without overlaps between different fibers (right).

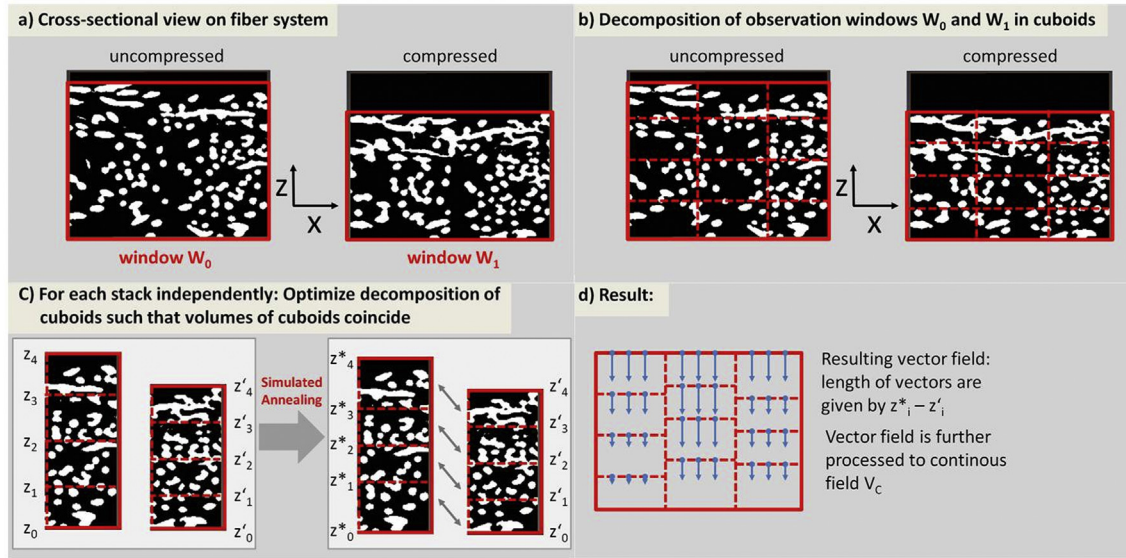


Fig. 8. Fitting the vector field of the compression model for fixed  $c$ .

microstructure. In other words, the 'optimal' decomposition  $S^*$  should fulfill the equality

$$S^* = \arg \min_{0=z_0 < \dots < z_n} \sum_{i=1}^n |V_i(z_0, \dots, z_n) - V_i^*|^2. \quad (1)$$

Thus, we have formulated an *optimization problem* and explain later on (in Section 3.2.2), how to solve it. Note that, since we assume that fibers are only translated in  $z$ -direction, it is sufficient to optimize each vertical stack of cuboids separately, see Fig. 8c. For the moment, let us assume that we have already obtained the optimal decomposition  $S^* = (z_0^*, \dots, z_n^*)$ . Then this gives us detailed information about the local compression: Each starting and end-points of the fiber segments (forming polygonal tracks) of the uncompressed fiber system that is located at point  $(x_j, y_k, z_i^*)$  should be translated by the vector given by  $(0, 0, z_i^* - z_i')^T$  according to the optimal decomposition  $S^*$ . Thus, the result of the optimal decomposition  $S^*$  is a set of translation vectors given on discrete points in the observation window  $W_0$ , see Fig. 8d.

To compute the 'optimal' vector field  $V_c$ , we fit a continuous and parametric function to these translation vectors by non-linear regression [29]. In particular, we first consider a suitable class of parametrized continuous vector fields  $\{V_c(x, y, z) : V_c(x, y, 0) = 0, \text{ and } V_c(x, y, z) \leq z \text{ for all } (x, y)^T \in \mathbb{R}^2\}$  such that no transitions beyond the observation window are made. Then, the parameters of the vector field are estimated by non-linear regression methods. For this, we use the surface fitting tool implemented in Matlab [30]. To check the quality of how the estimated continuous vector field fits the translation vectors given on discrete points in space, we consider the coefficient of determination  $R^2 \in [0, 1)$ . It is a measure for goodness-of-fit in terms of non-linear regression. The closer  $R^2$  is to 1 the better the regression model describes the given data. Note that  $R^2 > 0.9$  represents a very good fit [29], where a very good data fit means that the local distribution of fibers in the virtually compressed structure coincides with the distribution found in the image data of the experimentally compressed structure.

### 3.2.2. Simulated annealing

In order to solve the optimization problem described in (Section 1), we use *simulated annealing*, a well-know stochastic optimization

algorithm which numerically solves complex global optimization problems by means of Markov-Chain-Monte-Carlo simulation [31]. Roughly speaking, the basic idea of the simulated annealing algorithm is to start with some initial configuration, say  $(z_0^{(0)}, \dots, z_n^{(0)})$  and then randomly change one component of the vector. The change is accepted if the cost function (which measures the deviation of the fiber volumes within the uncompressed and compressed cuboids and which we aim to minimize) gets smaller. Otherwise, the change is only accepted with a certain probability and the next iteration step is started. The interesting aspect of simulated annealing is that it allows transitions which increase the cost function. This makes an 'escape' from local minima possible. The probability for accepting transitions that increase the cost function decreases with an increasing number of steps and is governed by a so-called cooling schedule.

We now explain the simulated annealing algorithm in more detail. Let the side length in  $z$ -direction of the cuboids of  $W_0$  be given by  $z'_0 = 0 < z'_1 < \dots < z'_n = z_{\max}$  and the corresponding side length of the fixed decomposition of  $W_1$  be given by  $z_0 = 0 < z_1 < \dots < z_n$ . Furthermore, we denote by  $\text{MSE}(z_0, \dots, z_n)$  the mean squared deviation of the volumes computed for corresponding cuboids given the decomposition of  $W_0$  by  $(z'_0, \dots, z'_n)$  and  $W_1$  by  $(z_0, \dots, z_n)$ , i.e.,

$$\text{MSE}(z_0, \dots, z_n) = \sum_{i=1}^n |V_i(z_0, \dots, z_n) - V_i^*|^2.$$

The simulated annealing algorithm has three parameters  $T > 0, M \in \mathbb{N}$  and  $g \in (0, 1)$ . Note that the triple  $(T, n, g)$  is called *cooling schedule*, see Ref. [31]. The algorithm works as follows, where we put  $z_0^{(0)} = z_0, \dots, z_n^{(0)} = z_n$ .

- (a) Set  $m = 1$  and repeat the steps (b) to (d) until  $m = M$  then go to (e).
- (b) Choose randomly one  $z_i^{(m-1)} \in \{z_1^{(m-1)}, \dots, z_n^{(m-1)}\}$  and put  $z_j^{(m)} = z_j^{(m-1)}$  for all  $j \in \{1, \dots, n\} \setminus \{i\}$ .
- (c) Modify  $z_i^{(m-1)}$  by adding a random number  $X \sim U(-0.01, 0.01)$ , i.e.,  $z_i^{(m)} = z_i^{(m-1)} + X$ . If  $z_i^{(m-1)} + X > z_{i+1}^{(m-1)}$  or  $z_i^{(m-1)} + X < z_{i-1}^{(m-1)}$ ,  $z_i^{(m)} = z_i^{(m-1)}$  and repeat step (c).

- (d) If  $\text{MSE}(z_0^{(m)}, \dots, z_n^{(m)}) < \text{MSE}(z_0^{(m-1)}, \dots, z_n^{(m-1)})$  accept the modification, otherwise accept only with a certain probability which is given by

$$\exp\left(-\left(\text{MSE}(z_0^{(m)}, \dots, z_n^{(m)}) - \text{MSE}(z_0^{(m-1)}, \dots, z_n^{(m-1)})\right)/T\right).$$

Set  $m = m + 1$  and continue with (b).

- (e) Set  $T = g \cdot T$ . If

$$\frac{|\text{MSE}(z_0^{(0)}, \dots, z_n^{(0)}) - \text{MSE}(z_0^{(M)}, \dots, z_n^{(M)})|}{\max\{\text{MSE}(z_0^{(0)}, \dots, z_n^{(0)}), \text{MSE}(z_0^{(M)}, \dots, z_n^{(M)})\}} < 0.0001$$

the algorithm terminates, otherwise set  $z_0^{(0)} = z_0^{(M)}, \dots, z_n^{(0)} = z_n^{(M)}$  and go to (a).

As initial value for  $T$  we choose  $T = 1 \cdot 10^{-6}$ , which is a value where enough changes are accepted. The number  $M$  of iterations per step is chosen equal to  $M = 10,000$ , and the factor  $g$  is put equal to  $g = 0.98$  as recommended in Ref. [31].

### 3.3. Validation of fitting procedure

In this section, we analyze the goodness of the fitting procedure for the continuous vector field  $V_c$  for fixed  $c \in [0, c_{\max})$  introduced in Section 3.2. Therefore, we generate uncompressed synthetic 3D fiber systems, using the stochastic model presented in Ref. [22]. Then, for a given vector field  $V_c$ , we virtually compress the synthetic fiber system using the compression model introduced in Section 3.1 and subsequently estimate the vector field  $\hat{V}_c$  from these uncompressed

virtual microstructures, as described in Section 3.2. Then, we compare the given vector field  $V_c$  to its estimated counterpart  $\hat{V}_c$ .

The parameters of the stochastic fiber model introduced in Ref. [22] are chosen such that the virtually generated fiber systems resemble the fiber systems of experimental (uncompressed) non-woven GDL, see Section 2. Note that the uncompressed (virtual) microstructures are simulated on the observation window  $W_0 = [0, 800] \times [0, 800] \times [0, 200]$  (i.e., dimensions of generated GDL structures), see also Fig. 9 (left).

The compressed microstructures are obtained by applying the compression model presented in Section 3.1, for a given vector field  $V_c$  to the simulated (uncompressed) fiber system. In particular, we consider two different vector fields  $V_c^{(1)}$  and  $V_c^{(2)}$ , where the first one is chosen as a linear vector field  $V_c^{(1)}(x, y, z) = 0.5 \cdot z$  which only depends on the  $z$ -component, whereas the second one is a vector field  $V_c^{(2)}(x, y, z) = z \cdot (0.3 - |x - 400| \cdot 0.0015)$  depending on the  $x$ - and  $z$ -components. Subsequently, we apply the compression model for these two vector fields to the synthetic uncompressed data and compare the fitted vector fields to the actual ones. Note that both vector fields  $V_c^{(1)}$  and  $V_c^{(2)}$  fulfill the properties of a vector field for the compression model, i.e., both are continuous, and it holds that  $V_c^{(i)}(x, y, 0) = 0$  and  $V_c^{(i)}(x, y, z) \leq z$  for  $i \in \{1, 2\}$ . The uncompressed microstructure generated by the stochastic 3D simulation model as well as the compressed microstructures gained by applying the compression model for the vector fields  $V_c^{(1)}$  and  $V_c^{(2)}$  to the uncompressed microstructures are visualized in Fig. 9.

Recall that by means of the fitting technique proposed in Section 3.2, estimates of the vector field  $V_c^{(i)}$  at discrete points in the observation window  $W_0$  are computed. Using the surface fitting tool implemented in Matlab [30], a given non-linear surface can be fitted to these estimates.

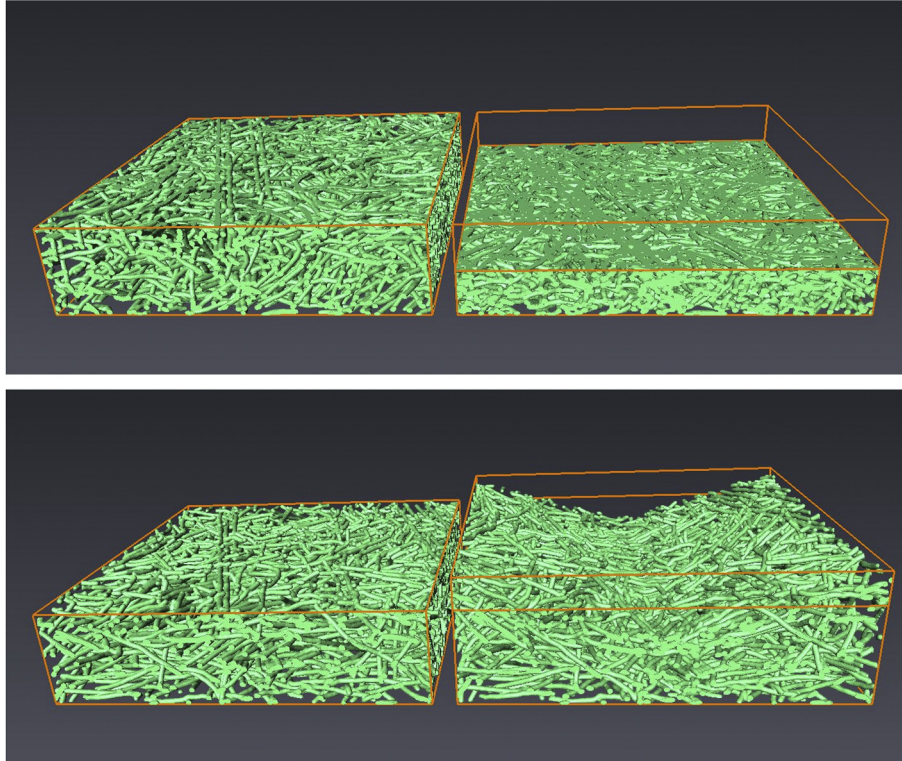


**Fig. 9.** Left column: realizations of two uncompressed microstructures drawn from the stochastic 3D simulation model; right column: compression model applied to the uncompressed microstructures (left) for the vector fields  $V_c^{(1)}$  (top) and  $V_c^{(2)}$  (bottom).

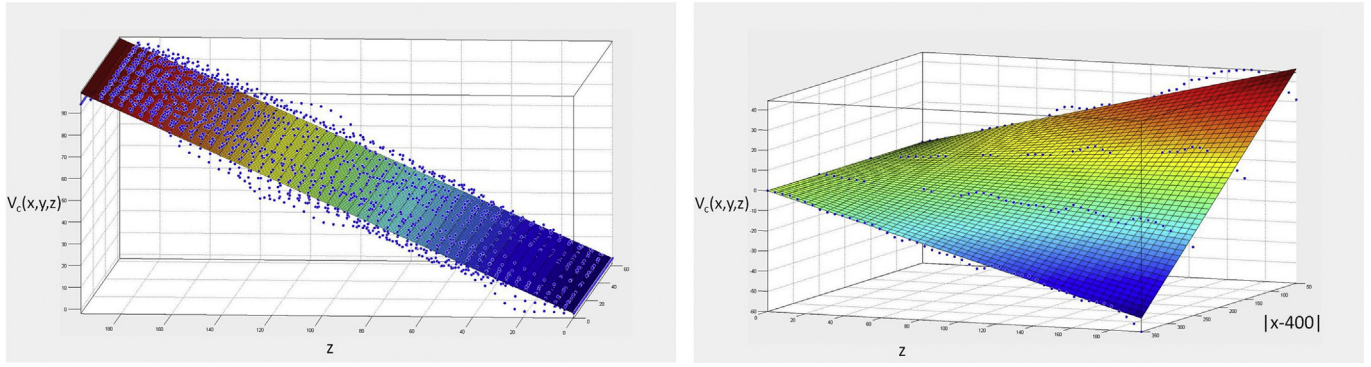


**Fig. 10.** The fitted vector fields  $\hat{V}_c^{(1)}$  (left) and  $\hat{V}_c^{(2)}$  (right) displayed by the surface, where the blue points are estimates of the vector field  $V_c^{(i)}$  at discrete points in the observation window  $W_0$  obtained by the simulated annealing algorithm. (For interpretation of the references to color in this figure legend, the reader is referred to the web version of this article.)

In Fig. 10, the result of the fitting procedure can be seen. For the first vector field  $V_c^{(1)}$ , we get an estimated vector field of  $\hat{V}_c^{(1)}(x, y, z) = 0.505 \cdot z$  and for the second vector field  $V_c^{(2)}$  an estimation of  $\hat{V}_c^{(2)}(x, y, z) = z \cdot (0.321 - |x - 400| \cdot 0.00169)$  is obtained. Thereby, the coefficients of determination  $R^2 = 0.977$  for  $\hat{V}_c^{(1)}$  and  $R^2 = 0.984$  for  $\hat{V}_c^{(2)}$  are achieved. Thus, by the fitting procedure introduced in Section 3.2, it is possible to estimate the vector field of a uniaxial compression almost perfectly.

### 3.4. Arbitrary compression rates $c$

In Sections 3.1 and 3.2, a toolbox has been introduced which consists of a model to describe microstructures of fiber-based materials under compression and a procedure to estimate the vector field  $V_c$  of the compression model for a specified compression rate  $c$ . Therefore, the uncompressed and one single compressed microstructure of a fiber-based material have to be given. Thus, it is possible to describe the microstructural changes from the uncompressed to the compressed microstructure for one single rate of compression  $c$ . Note however that at the present stage it is not yet possible to describe the compression process for arbitrary rates of compression  $c \in [0, c_{\max}]$ .

The basic idea to obtain a compression model for arbitrary rates of compression is as follows: First, let us suppose that an uncompressed and  $m$  compressed microstructures with compression rates  $c \in \{c_1, \dots, c_m\}$  are available. For each  $c \in \{c_1, \dots, c_m\}$ , we estimate the corresponding vector field  $V_c$  by means of the fitting technique which was introduced in Section 3.2. Assuming that  $\{V_c, c \in [0, c_{\max}]\}$  is a function of  $c$ , this gives us  $m$  points of support of  $V_c$  (i.e.  $\{\hat{V}_{c_1}, \dots, \hat{V}_{c_m}\}$ ) and by subsequently applying regression techniques we obtain a set of vector fields  $\{V_c, c \in [0, c_{\max}]\}$ .

More precisely, the compression of the GDL is managed by the family of continuous vector fields  $\{V_c, c \in [0, c_{\max}]\}$  which is described by some parameters  $(p_1, \dots, p_n)$ , i.e.,  $V_c = V_c^{(p_1, \dots, p_n)}$ . Since the vector fields depend on the compression rate, we interpret the

parameter vector  $(p_1, \dots, p_n)$  as a function of the compression rate  $c$ , i.e.

$$\begin{aligned} (p_1, \dots, p_n)^T &: [0, 1] \rightarrow \mathbb{R}^n \\ c &\mapsto (p_1(c), \dots, p_n(c))^T \end{aligned} \quad (2)$$

For each pair of uncompressed and compressed microstructure, the parameters  $(p_1, \dots, p_n)$  of the same parametric vector field  $V_c^{(p_1, \dots, p_n)}$  are fitted using the estimation method introduced in Section 3.2. This yields  $m + 1$  points of support for the function  $(p_1, \dots, p_n)$ , i.e., we obtain  $(\hat{p}_1(c), \dots, \hat{p}_n(c))$  for  $c \in \{0, c_1, \dots, c_m\}$ . Based on these fitted values we describe the dependency of the compression rate  $c$  on the individual parameters  $p_i$  by a function  $p_i(c)$ , where  $p_i(c)$  is computed by means of non-linear regression. The vector field  $V_c$  which uniquely determines the compression model is then given by  $V_c^{(p_1(c), \dots, p_n(c))}$ .

## 4. Application to experimental data

To begin with, we apply the compression model introduced in Section 3 to the experimental image data of non-woven GDL in PEMFC which have been described in Section 2. In particular, as data basis, we consider experimental 3D image data of non-woven GDL without compression ( $c = 0$ ) and for three different compression rates  $c \in \{10, 20, 30\}$  (in %). The goal in this section is to use the model introduced in Section 3 in order to describe the compression of fiber systems of non-woven GDL in PEMFC for arbitrary rates of compression  $c \in [0, c_{\max}]$ . Finally, we validate the compression model for arbitrary rates of compression by comparing structural characteristics computed for experimentally and virtually compressed microstructures.

### 4.1. Estimation of vector fields

Suppose that experimental 3D image data of compressed fiber systems for compression rates  $c \in \{0, 10, 20, 30\}$  (in %) are available, see Figs. 3 and 4. In the following, we distinguish between two kinds of compression, i.e., using a flat stamp and a stamp possessing

**Table 1**  
Estimated coefficients of  $p_i(c) = a_i(\exp(b_i c) - \exp(d_i c))$  for  $i \in \{2, \dots, 6\}$ .

	$i = 2$	$i = 3$	$i = 4$	$i = 5$	$i = 6$
$a_i$	−0.235	0.041	0.784	$-1.282 \cdot 10^{-5}$	−0.305
$b_i$	−1.911	0.347	−7.583	−1.150	−1.666
$d_i$	−16.14	0.316	−7.627	−20.15	−1.666

**Table 2**  
Coefficient of determination  $R^2$  computed for the fitted vector fields of the compression model applied to experimental non-woven GDL data for different rates of compression  $c$  and stamp geometries.

	$c = 10$	$c = 20$	$c = 30$
Flat stamp	0.93	0.97	0.96
Flow-field stamp	0.95	0.96	0.97

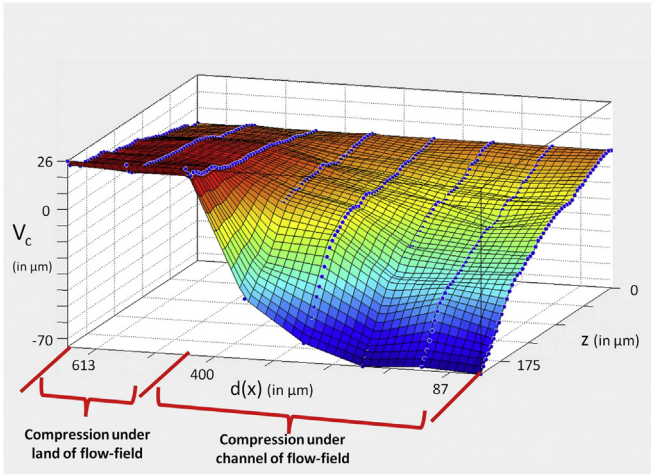


**Fig. 11.** Blue points: estimated transition vectors by the fitting technique introduced in Section 3.2 and applied to the 10% compressed GDL by a flow-field stamp. Surface: linear interpolation between these points. (For interpretation of the references to color in this figure legend, the reader is referred to the web version of this article.)

a flow-field structure, see Fig. 1. For each type of stamp, we separately apply the fitting technique introduced in Section 3.4 in order to describe the microstructure of GDL compressed by an arbitrary rate of compression. Recall that the uncompressed, experimental GDL is given in a domain size  $1314 \times 1314 \times 200 \mu\text{m}^3$  for the series of images which are compressed by a flat stamp, and  $1314 \times 1314 \times 210 \mu\text{m}^3$  for the flow-field stamp.

#### 4.1.1. Flat stamp

In case of the flat stamp, we choose  $n = 1$  in (Section 3.4), and  $V_c^{(p_1(c))}(x, y, z) = p_1(c) \cdot z$ . Table 2 illustrates that the choice of this parametric form is reasonable since the coefficients of determination  $R^2$  are very close to 1. Moreover, it turns out that the function  $p_1(c) = 1 - c$  is a suitable choice, see Fig. 12 (left). Thus, for the flat stamp,  $\{V_c, c \in [0, c_{\max}]\}$  is given by  $V_c(x, y, z) = (1 - c)z$  for  $c \in [0, c_{\max}]$ . In other words, by compressing GDL using a flat stamp, fibers are translated linearly according to their locations with respect to the  $z$ -coordinate. Note that in fact, this behavior is intuitive but it was never shown before and often used as model assumption, see e.g. Ref. [20].

#### 4.1.2. Flow-field stamp

In the next step, we consider the estimation of the parametrized vector field  $V_c$  for compression by a flow-field stamp. First note that

the channel of the flow-field stamp has a width of  $w = 790 \mu\text{m}$ . Since the profile of the flow-field stamp replicates in  $y$ -direction, we assume that the vector field  $V_c$  for compression by a flow-field stamp does not depend on the  $y$ -coordinate, but on the orthogonal distance  $d(\cdot)$  (given in  $\mu\text{m}$ ) to the center of the flow-field channel (orientated in  $(0, 1, 0)^T$  direction as displayed in Fig. 4). Note that the estimated vector field contains all information to describe the transition of fibers caused by the compression. Hence, all structural changes of microstructures that occur by the uniaxial compression can be explained by means of the vector field. To get an idea for the choice of the parametrized vector field  $V_c$  concerning compression by a flow-field stamp, consider Fig. 11. In this figure, we see that fibers underneath the ribs of the flow-field (i.e. fibers with  $d(x) > w/2$ ) are translated linearly according to their locations with respect to the  $z$ -coordinate. But fibers underneath the channel of the flow-field (i.e. fibers with  $d(x) < w/2$ ) follow a non-linear translation rule. Note that values of  $V_c$  smaller than zero indicate decompression of the fibers. Thus, fibers located close to the center of the flow-field channel are decompressed, see Fig. 11. Moreover, we observe that the decompression of fibers within the flow-field channel is smaller (larger) the closer the fibers are located to the bottom (top) of the GDL. Thus, in this case the continuous vector field  $V_c$  is constructed by distinguishing between the two disjoint regions and describe the translation of fibers in those regions, separately. To assure the continuity of  $V_c$ , we include a small transition region ( $d(x) \in [w/2 - 4, w/2]$ ) connecting regions 1 and 2, linearly. Thus, for the parametric vector field  $V_c$ , it seems reasonable (see Table 2) to put  $n = 6$  and consider the set-up

$$V_c^{(p_1(c), \dots, p_6(c))}(x, y, z) = g_1(z; c) \mathbb{1}_{d(x) \geq \frac{w}{2}} + \left( g_1(z; c) + \left( \frac{g_1(z; c) - g_2(\frac{w}{2} - 20, z; c)}{20} \right) \cdot \left( d(x) - \frac{w}{2} \right) \right) \mathbb{1}_{\frac{w}{2} - 20 < d(x) < \frac{w}{2}} + g_2(x, z; c) \mathbb{1}_{d(x) \leq \frac{w}{2} - 20},$$

where

$$g_1(z; c) = p_1(c) \cdot z, \\ g_2(d(x), z; c) = p_2(c)z + p_3(c)d(x)z + p_4(c)z^2 + p_5(c)z^3 + p_6(c)d(x)^2z^2$$

and  $c \in [0, c_{\max}]$ . Moreover, we put  $p_1(c) = 1 - c$  and for  $i \in \{2, \dots, 6\}$  we use the family of equations  $p_i(c) = a_i(\exp(b_i c) - \exp(d_i c))$ , where the estimated coefficients are specified in Table 1. Table 2 and Fig. 12 (right) illustrate that the choice of  $V_c$  seems to be adequate.

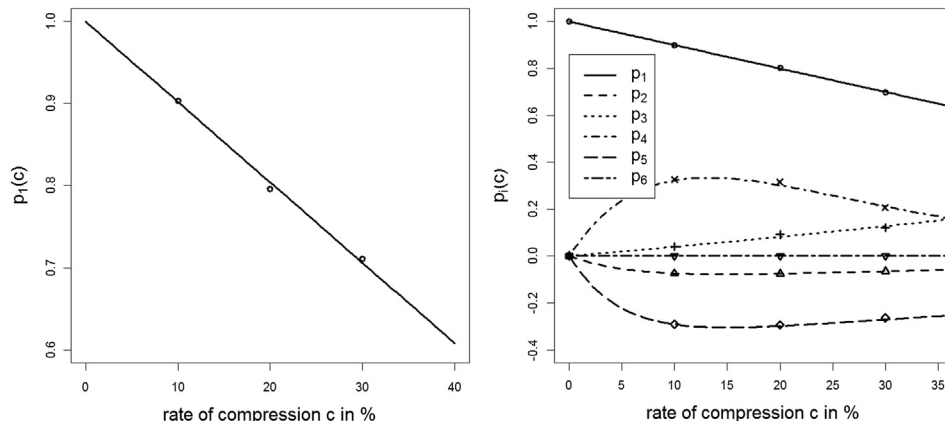


**Fig. 12.** Fitted functions  $p_i(c)$  for the compression by a flat stamp (left) and a flow-field stamp (right), where  $p_2, \dots, p_6$  are appropriate scaled in order to check the goodness of fit.

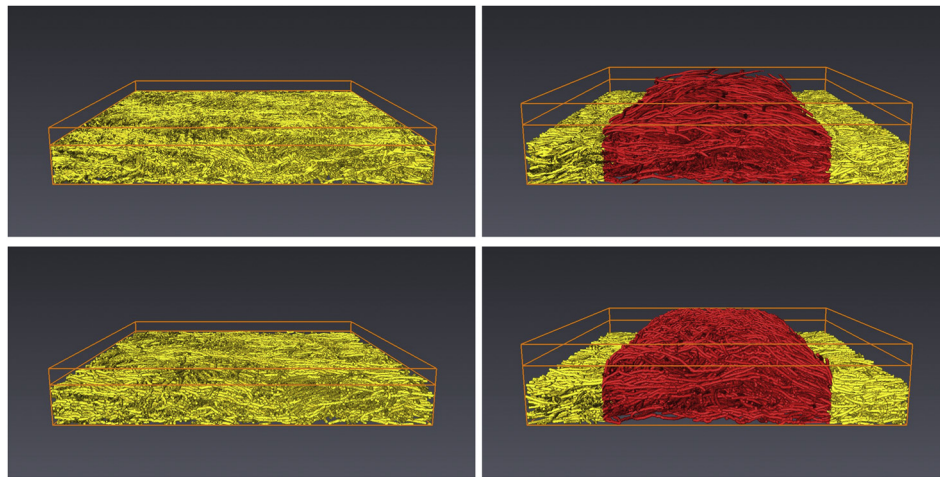


**Fig. 13.** First row: experimental 3D image data of non-woven GDL compressed by flat stamp (left) and by a flow-field stamp (right) with compression rate  $c = 30\%$ ; second row: extracted fiber system virtually compressed by a flat stamp (left) and by a flow-field stamp (right) using the compression model with compression rate  $c = 30\%$ .

#### 4.2. Validation of compression model

In Section 4.1, vector fields of the compression model for compression by a flat stamp and a stamp with flow-field structure are estimated in order to describe compressed microstructures of non-woven GDL in PEMFC for arbitrary compression rates  $c \in [0, c_{\max})$ . We now check if the compression model reproduces the microstructures of compressed non-woven GDL for the two stamp types sufficiently well. More precisely, to generate the virtually compressed microstructures we first consider the extracted fiber system of the uncompressed GDL, see Section 2.3. Subsequently, the extracted fibers are translated by the compression model with the help of the estimated vector fields for the compression rates  $c \in \{0, 10, 20, 30\}$  (in %), computed in Section 4.1.

From Fig. 13 it can be seen that the virtually compressed images coincide quite nicely with the synchrotron images of experimentally compressed materials. In addition to visual comparison we check the goodness-of-fit more formally. That means, the compression model is validated by comparing structural characteristics computed for experimentally compressed and virtually compressed microstructures.

In particular, for each compression rate  $c$ , we compare the *porosity* and the *mean spherical contact distance* for experimentally compressed and virtually compressed microstructures. Note that the porosity of a 3D microstructure given in an observation window  $W$  is defined as the volume of the pore phase divided by the volume of  $W$ . Moreover, the mean spherical contact distance is the mean value of the closest distances from all points located in the pore phase to the fiber phase. When describing the properties of porous materials the spherical contact distance is of high significance.

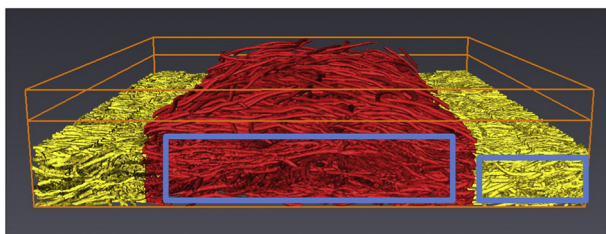


**Fig. 14.** The blue boxes display the decomposition in two quite homogeneous sub-regions, i.e., a channel and a land region. (For interpretation of the references to color in this figure legend, the reader is referred to the web version of this article.)

Since it describes the spatial (micro-) structure of the pore phase this information is closely related to the pore size distribution. The influence of compression on pore size distribution and the possible consequences for mass transport are discussed in more detail in the recent paper [23]. Since the microstructures compressed by a flat stamp are homogeneous, the porosity and the mean spherical contact distance are computed in the whole observation window. The microstructures compressed by a stamp with flow-field structure can be decomposed in two quite homogeneous sub-regions: the region underneath the flow-field channel and the region underneath the ribs of the flow-field, see the blue boxes in Fig. 14. Thus, for each sub-region separately, the porosity and the mean spherical contact distance are computed. The results of comparing structural characteristics for experimentally compressed and virtually compressed microstructures can be seen in Fig. 15. For both types of stamps a good agreement is found. Note that this also justifies the model assumption of the compression model, i.e., that fibers are only translated in  $z$ -direction (the direction of the uniaxial compression). Re-considering Fig. 15 we clearly see that the porosity (mean spherical contact distance) computed for the samples compressed by a flat stamp and underneath the land regions when referring to compression by a flow-field stamp decreases (increases) linearly with respect to the compression rate. In contrast, the porosity (mean spherical contact distance) underneath the channel regions of samples compressed by a flow-field stamp shows a non-linear behavior. This can be explained by the computed vector fields considered in the previous section where underneath the land (channel) of the flow-field a linear (non-linear) translation of fibers is observed. Note that the focus of the present paper is on the introduction of a compression model which is capable to generate microstructures of GDL with an arbitrary degree of compression in very large volumes taking into account the influence of the flow-field geometry. Changes in the microstructure that result from compression and possible consequences for the fuel cell operation are discussed in more detail in the recent paper [23].

#### 5. Application to simulated data

In addition to the scenarios considered in Section 4, the compression model can be applied not only to experimental data but also to virtual non-woven GDL data sampled from stochastic microstructure models. The main advantages of virtual GDL are that

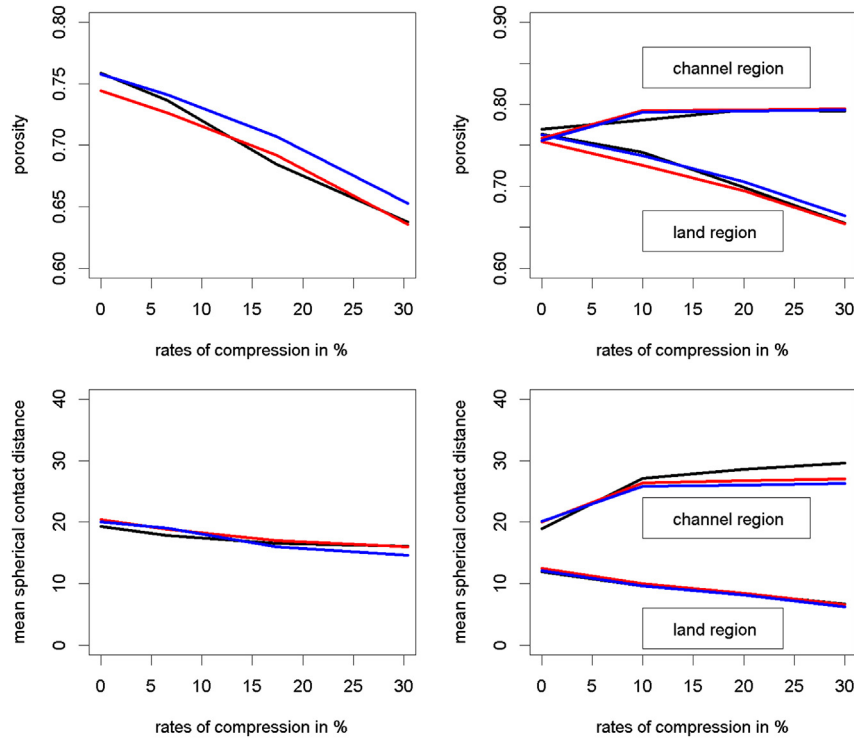


**Fig. 15.** Validation of compression model by comparing the porosities (top) and the mean spherical contact distances (bottom) computed for the experimentally compressed image data (black lines), for data generated by virtually compressing the extracted fiber systems (red lines) and for data gained by compressing virtual non-woven GDL by the compression model (blue lines), where we distinguish between compression by a flat stamp (left) and a flow-field stamp (right). (For interpretation of the references to color in this figure legend, the reader is referred to the web version of this article.)

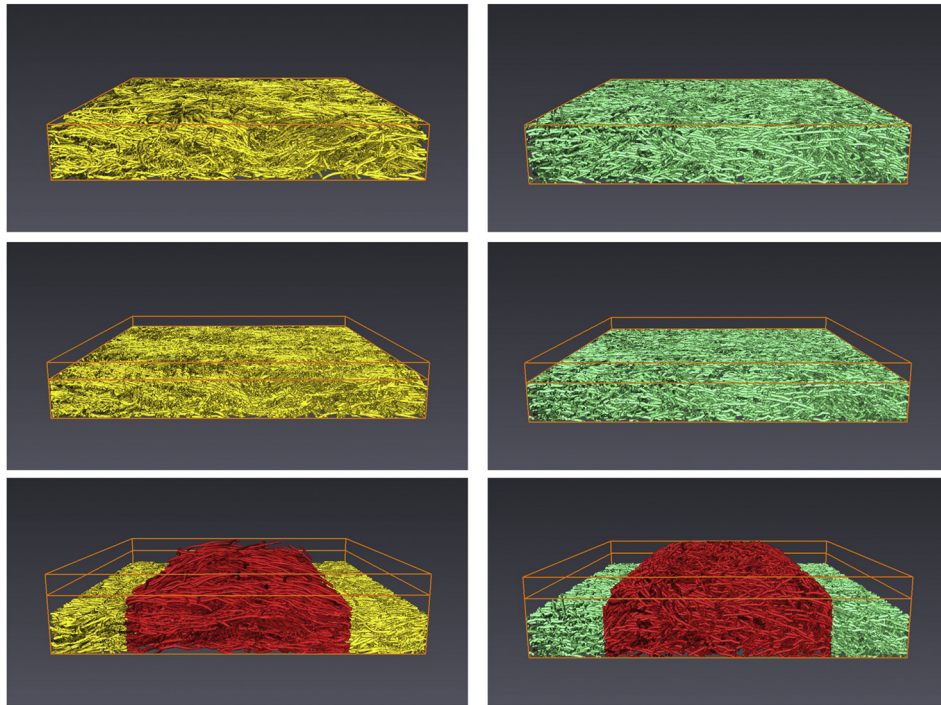


**Fig. 16.** First row: experimental (left) and synthetic (right) uncompressed non-woven GDL data; second row: non-woven GDL data compressed by a flat stamp (with compression rate  $c = 30\%$ ) experimentally (left) and using the compression model (right); third row: non-woven GDL data compressed by a flow-field stamp (with compression rate  $c = 30\%$ ) experimentally (left) and applying the compression model on a virtual fiber system sampled from the stochastic non-woven GDL model (right).

they can be produced in arbitrarily large observation windows with arbitrarily many replications and that their generation is cost- and time-saving. Moreover, by systematically varying the parameters of the stochastic microstructure model, new virtual GDL can be produced and in combination with computational transport simulations, microstructure and functionality relationships of the GDL can be investigated. Thus, after the estimation of the vector fields as discussed in Section 4.1, the compression models for flat stamps and stamps with flow-field structure are applied to (uncompressed) virtual non-woven GDL. For the generation of the (uncompressed) virtual non-woven GDL a stochastic simulation model is used which has recently been developed in Ref. [22]. In particular, it has been shown in Ref. [22] that transport-relevant characteristics are captured by the microstructure model quite well. Thus, simulated 3D microstructures drawn from the model proposed in Ref. [22] can be seen as realistic representations of experimental uncompressed GDL. The combination of this stochastic simulation model with the compression model proposed in the present paper can be interpreted as a stochastic 4D model which describes continuously compressed 3D microstructures of non-woven GDL in PEMFC for arbitrary compression rates  $c \in [0, c_{\max}]$ .

By comparing the same structural characteristics as considered in Section 4 we validate the 4D model, i.e., we check if the stochastic 4D compression model describes experimentally compressed microstructures of non-woven GDL adequately. As shown in Fig. 15, a very good accordance between these characteristics is found. Additionally, there is a nice visual accordance of experimental 3D image data of compressed non-woven GDL and the virtually compressed non-woven GDL sampled from the stochastic simulation model proposed in Ref. [22] in combination with the compression model introduced in the present paper, see Fig. 16.

## 6. Conclusions

We have introduced a novel parametrized model that describes the 3D microstructure of compressed fiber-based materials. Given the input of a 3D microstructure of some fiber-system, the model compresses the system of fibers in a uniaxial direction for arbitrary compression rates. The compression model was applied to non-woven GDL in PEMFC and subsequently validated by comparing structural characteristics computed for experimentally compressed and virtually compressed microstructures, where two kinds of compression – using a flat stamp and a stamp with flow-field profile – were considered. For both types of stamps, an excellent agreement between experimental compression and virtual compression was found. In addition, the compression model was combined with a stochastic model for uncompressed non-woven GDL. This allows to generate virtual GDL in arbitrarily large volumes with arbitrarily many replications and with low computational efforts. Thus, by systematically varying the parameters of these combined models, new virtual GDL can be generated and in combination with computational transport simulations, the microstructure-functionality relationship of the GDL can be investigated. Currently, the compression model is used for virtual scenario analyzes with the general aim to quantify the effect of compression using a stamp with a flow-field structure compared to compression by a flat stamp. The results of this ongoing research will be reported in a forthcoming paper. But note that the presented

compression model is very flexible and can thus be applied to various problems not only in the field of GDL in PEMFC.

## Acknowledgments

We gratefully acknowledge funding of the present research by the German Federal Ministry for Education and Science (BMBF) in the framework of the priority program ‘Mathematics for Innovations in Industry and Services’ under grant numbers 03MS607A, 03MS607B and 03MS607C.

## References

- [1] C. Hartnig, L. Jörissen, J. Kerres, W. Lehnert, J. Scholta, in: M. Gasik (Ed.), *Materials for Fuel Cells*, Woodhead Publishing, Cambridge, 2008, pp. 101–184.
- [2] G. Hoogers (Ed.), *Fuel Cell Technology Handbook*, CRC Press LLC, Boca Raton, 2012.
- [3] C. Hartnig, L. Jörissen, J. Kerres, W. Lehnert, J. Scholta, in: M. Gasik (Ed.), *Materials for Fuel Cells*, Woodhead Publishing, Cambridge, 2008, pp. 101–184.
- [4] K. Jia, X. Li, *Prog. Energy Combust. Sci.* 37 (2011) 221–291.
- [5] M.F. Mathias, J. Roth, J. Fleming, W. Lehnert, in: W. Vielstich, A. Lamm, H. Gasteiger (Eds.), *Handbook of Fuel Cells*, J. Wiley & Sons, London, 2003, pp. 517–537.
- [6] C.-Y. Wang, *Chem. Rev.* 104 (2004) 4727–4766.
- [7] N. Zamel, X. Li, *Prog. Energy Combust. Sci.* 39 (2013) 111–146.
- [8] W. Vielstich, A. Lamm (Eds.), *Handbook of Fuel Cells – Fundamentals, Technology and Applications*, J. Wiley & Sons, Chichester, 2003.
- [9] S. Litster, D. Sinton, N. Djilali, *J. Power Sources* 154 (2006) 95–105.
- [10] P.K. Sinha, P. Halleck, C.-Y. Wang, *Electrochem. Solid-State Lett.* 9 (2006) A344–A348.
- [11] H. Markötter, I. Manke, P. Krüger, T. Arlt, J. Haussmann, M. Klages, H. Riesemeier, C. Hartnig, J. Scholta, J. Banhart, *Electrochem. Commun.* 13 (2011) 1001–1004.
- [12] R. Alink, J. Haußmann, H. Markötter, M. Schwager, I. Manke, D. Gerteisen, *J. Power Sources* 233 (2013) 358–368.
- [13] H.-M. Chang, C.-W. Lin, M.-H. Chang, H.-R. Shiu, W.-C. Chang, F.-H. Tsau, *J. Power Sources* 196 (2011) 3773–3780.
- [14] J. Ge, A. Higier, H. Lui, *J. Power Sources* 156 (2006) 922–927.
- [15] A.C. Olesen, T. Berning, S.K. Kær, *J. Fuel Cell Sci. Technol.* 9 (2012) 031010–031011.
- [16] Z. Shi, X. Wang, L. Guessous, *J. Fuel Cell Sci. Technol.* 7 (2010) 021012–021021.
- [17] Y. Gao, X. Zhang, P. Rama, R. Chen, H. Ostadi, K. Jiang, *J. Fuel Cell Sci. Technol.* 9 (2012) 041010–041011.
- [18] J. Becker, R. Flückiger, M. Reum, F.N. Büchi, F. Marone, M. Stampanoni, *J. Electrochem. Soc.* 156 (2009) B1175–B1181.
- [19] D. Froning, J. Brinkmann, U. Reimer, V. Schmidt, W. Lehnert, D. Stolten, *Electrochim. Acta* 110 (2013) 325–334.
- [20] V.P. Schulz, J. Becker, A. Wiegmann, P.P. Mukherjee, C.Y. Wang, *J. Electrochem. Soc.* 154 (2007) B419–B426.
- [21] G. Gaiselmann, I. Manke, W. Lehnert, V. Schmidt, *Image Anal. Stereol.* 32 (2013) 57–63.
- [22] G. Gaiselmann, D. Froning, C. Tötze, C. Quick, I. Manke, W. Lehnert, V. Schmidt, *Int. J. Hydrogen Energy* 38 (2013) 8448–8460.
- [23] C. Tötze, G. Gaiselmann, M. Osenberg, J. Böhner, T. Arlt, H. Markötter, A. Hilger, F. Wieder, A. Kupsch, B.R. Müller, M.P. Hentschel, J. Banhart, V. Schmidt, W. Lehnert, I. Manke, *J. Power Sources* 253 (2014) 123–131.
- [24] W. Görner, M.P. Hentschel, B.R. Müller, H. Riesemeier, M. Krumrey, G. Ulm, W. Diete, U. Klein, R. Frahm, *Nucl. Instrum. Methods Phys. Res. Sect. A* 467–468 (Part 1) (2001) 703–706.
- [25] J. Banhart, A. Borbely, K. Dzieciol, F. Garcia-Moreno, I. Manke, N. Kardjilov, A.R. Kayser-Pyzalla, M. Strobl, W. Treimer, *Int. J. Mater. Res.* 101 (2010) 1069–1079.
- [26] J.H. Kinney, M.C. Nichols, *Annu. Rev. Mater. Sci.* 22 (1992) 121–152.
- [27] S.H. Williams, A. Hilger, N. Kardjilov, I. Manke, M. Strobl, P.A. Douissard, T. Martin, H. Riesemeier, J. Banhart, *J. Instrum.* 7 (2012) P02014.
- [28] H. Altendorf, D. Jeulin, *Phys. Rev. E* 83 (2011) 041804.
- [29] D.M. Bates, D.G. Watts, *Nonlinear Regression Analysis and its Applications*, J. Wiley & Sons, New York, 1988.
- [30] Matlab Works, 2013, <http://www.mathworks.com/>.
- [31] P.J.M. Laarhoven, E.H.L. Aarts, *3D Simulated Annealing: Theory and Applications*, Kluwer Academic Publisher, Dordrecht, 1987.